Effect of post-annealing on the thermal stability and residual stresses in CVD (Al,Ti)N coatings investigated by in situ synchrotron diffraction

International Journal of Refractory Metals and Hard Materials 124 (2024) 106810

Contents lists available at ScienceDirect

International Journal of Refractory Metals and Hard Materials

journal homepage: www.elsevier.com/locate/IJRMHM

Effect of post-annealing on the thermal stability and residual stresses in CVD (Al,Ti)N coatings investigated by *in situ* synchrotron diffraction

Kristine Bakken [a], Olof Bäcke [a], Samik Roy Moulik [a], Andreas Stark [b], Thorsten Manns [c], Dirk Stiens [c], Mats Halvarsson [a], Magnus Hörnqvist Colliander [a,*]

[a] Department of Physics, Chalmers University of Technology, Gothenburg, Sweden
[b] Institute of Materials Physics, Helmholtz-Zentrum Hereon, Geesthacht, Germany
[c] Walter AG, Tübingen, Germany

ARTICLE INFO

Keywords:
Synchrotron X-ray diffraction
TEM
Spinodal decomposition
Phase transformation
Hexagonal AlN

ABSTRACT

The stress in thin wear resistant coatings is of great importance for the performance and service life of tools for metal cutting. In this work we have performed detailed investigations of the phase stability and temperature-dependent residual stresses in Al-rich $Al_xTi_{1-x}N$ ((Al,Ti)N) coatings deposited by chemical vapor deposition (CVD) on cemented carbide substrates. One as-deposited (Al,Ti)N coating and one coating post-annealed at 850 °C for 3 h were heated to 1200 °C while the structure and residual stresses were monitored by *in situ* high energy synchrotron X-ray diffraction. In the as-deposited state, the coating is in tensile stress at room temperature, but post-annealing resulted in a reduction of the room temperature residual stress. This lowering can be explained by growth of hexagonal AlN (hAlN) at the (Al,Ti)N grain boundaries during the isothermal hold time. Upon heating, the temperature-dependence of the residual stresses in both coatings are initially controlled by the mismatch in coefficients of thermal expansion (CTE) with the substrate, which leads to compressive stresses at typical service temperatures. Decomposition starts gradually at around 850–900 °C, resulting in an accelerated development of large compressive stresses with increasing temperatures, until the entire coating is transformed at temperatures just below 1100 °C. The growth of hAlN initiates slightly higher in temperature after post-annealing, whereas the upper limit for complete transformation remains unaffected. The lowered room temperature tensile stress after post-annealing leads to higher compressive stress at service temperatures, which is expected to improve the performance and service time of the coated tool.

1. Introduction

Al-rich $Al_xTi_{1-x}N$ ((Al,Ti)N) coatings are widely used today as hard protective coatings for cutting tools due to their excellent wear and oxidation resistance in combination with good chemical stability. [1–3] (Al,Ti)N coatings with a metastable face centred cubic (FCC) structure have traditionally been deposited onto cemented carbide substrates by physical vapor deposition (PVD), where the mechanical and chemical properties tend to improve as more Al is incorporated in the solid solution. The main challenge with the (Al,Ti)N coatings from PVD, is the solubility limit of Al around x = 0.67–0.7, as higher Al-content results in an undesirable hexagonal AlN (hAlN) phase. [4–6] Decreased hardness have been reported for mixed cubic (Al,Ti)N and hAlN coatings, [7,8] as well as inferior oxidation resistance, [9,10] compared to single phased cubic (Al,Ti)N coatings. The Al solubility limit is possible to overcome by another deposition method. Low pressure chemical vapor deposition (LP-CVD) has demonstrated the ability to produce metastable cubic (Al,Ti)N coatings with Al-contents as high as x = 0.9. [8,11,12] These coatings can be grown to a complex microstructure consisting of large, elongated grains extended through the coating thickness, and heterogenous chemical composition in the form of Ti-rich and Al-rich nanolamellae within the grains. [13–17] The lamella thicknesses typically are in the range 5–10 nm. [15,17,18] Approximate stoichiometries of $Al_{0.5}Ti_{0.5}N$ and $Al_{0.9}Ti_{0.1}N$, for the Ti-rich and Al-rich lamellae respectively, have been reported for coatings with an overall stoichiometry of $Al_{0.8}Ti_{0.2}N$, [17–19] but atom probe tomography has revealed large variations in the chemical composition also within the lamellae. [18,20]

The intricate microstructure and chemical inhomogeneity in the nanolamellar (Al,Ti)N CVD coatings give rise to complex spinodal decomposition and transformation reactions. *Ex situ* X-ray diffraction on

* Corresponding author.
E-mail address: magnus.colliander@chalmers.se (M. Hörnqvist Colliander).

https://doi.org/10.1016/j.ijrmhm.2024.106810
Received 26 June 2024; Received in revised form 17 July 2024; Accepted 17 July 2024
Available online 24 July 2024

coatings [8,16–19] and *in situ* X-ray diffraction on coatings [7] and powders [18,21], in combination with electron microscopy and other complementary techniques have been used to understand the decomposition mechanisms. However, there are large deviations in the reported temperature ranges for the reactions between different studies, spanning from start of hAlN formation below 850 °C to full decomposition only being achieved after annealing at 1200 °C for a prolonged period of time. [7,8,16–19] The temperature discrepancies reported in the literature are likely due to different processing and experimental conditions and prove the metastable nature of the (Al,Ti)N coatings, where the thermal stability and mechanical properties are governed not only by thermodynamics but also kinetics. Still, there seems to be a consensus; at elevated temperature hexagonal AlN starts to form at the (Al,Ti)N grain boundaries, but the early spinodal decomposition and cubic-to-hexagonal AlN transformation is restricted by the associated large volume expansion. Bäcke et al. reported that an (Al,Ti)N coating annealed for 3 h at 850 °C had very limited, but still identifiable, discrete domains of hAlN at the grain boundaries, which were more pronounced if the coating was annealed at 900 °C for 3 h. [17] This is in agreement with the observations of Tkadletz et al., where small amounts of hAlN were present in the as-deposited coating and no significant change was seen after annealing at 900 °C for 5 min. [18] By further increasing the temperature, bulk transformation of the coating into hAlN and cubic TiN occurs, where the transformation front moves from the surface, through the grains and inwards to the substrate. Bäcke et al. reported bulk transformation to begin slowly around 900 °C and more evident at 950 °C, but full decomposition is only achieved after annealing for 3 h at 1000 °C, resulting in complete removal of the lamella structure. [17] Tkadletz et al. described the spinodal decomposition to initiate around 1000 °C [7,18] in the Ti-rich lamellae with growth of cubic AlN clusters until a critical size is reached, where the whole coating transforms at once, since the Al-rich lamellae are no longer epitaxially stabilized by the Ti-rich lamellae. [7] The fully decomposed microstructure was reported to consist of discrete TiN particles embedded in a hAlN matrix. [7,18] However, a thin (Al,Ti)N layer at the interface to the TiN bottom layer of a few hundred nanometres has been reported to remain in some cases, even after prolonged exposure to high temperatures. [17,18]

The residual stresses are of interest because of their impact on various coating properties such as adhesion, fracture toughness, hardness, and lifetime of the inserts. [22] For cutting tools, compressive residual stresses are preferred as they are known to improve mechanical properties and delay crack initiation and propagation. [22] Moreover, as-deposited PVD $Al_{0.55}Ti_{0.45}N$ coatings on cemented carbide inserts fabricated with intermediate levels of compressive stress (0–3 GPa) have been shown to give the best cutting performance and the longest tool life, when compared to coatings with higher compressive stresses and coatings with tensile stress. [23] To ensure compressive stresses in the (Al,Ti)N coatings, post-treatment of the as-deposited coatings, such as dry or wet particle blasting or annealing is routinely done. The effect of post-annealing will depend on the temperature and time, as spinodal decomposition and transformation reactions will occur at elevated temperatures. However, increased hardness in the (Al,Ti)N coatings have been observed for coatings with small amounts of hAlN precipitation, due to the resulting compressive stresses, reminiscent of age hardening effects. [7] Tkadletz et al. performed *in situ* heating experiments using synchrotron X-ray diffraction and calculated the macroscopic strain developed in the (Al,Ti)N coating during annealing. Their findings show that at room temperature, the macroscopic strain corresponds to a tensile stress of 1.45 GPa, reaching a minimum of −2 GPa (compressive stress) at 1000 °C caused by the hAlN precipitation at the grain boundaries. [7] The same temperature also indicated the border between age hardening and over averaging, by the peak in coating hardness of 36.5 GPa. [7] Post-annealing can also give relaxation in the coating, demonstrated by Todt et al., who investigated the in-depth stress profile of $Al_{0.95}Ti_{0.05}N$ coatings with cross-sectional nanodiffraction. [8] The cubic (Al,Ti)N phase has a rapid stress increase from around −2 GPa (compressive) at the surface of the coating, to an equilibrium value of −0.3 GPa 2 μm into the coating. After annealing at 1050 °C the stress no longer depended on the depth but had a constant value around −1.5 GPa (compressive). [8] The same trend was seen for the hAlN phase. Another interesting aspect of the role of residual stresses is the one reported in the related (Al,Cr)N-based coating systems. It was shown that the stress state of the coating determines the onset of the spinodal decomposition and transformation reactions, where the reactions were delayed until a certain composition dependent value of residual stress was exceeded in the coating. [24,25] While residual stresses are expected to play a crucial role in (Al,Ti)N coatings, their assessment is typically limited to room temperature measurements, with little exploration into their temperature dependence, possibly due to the complexity of such measurements. Notable exceptions are the work by Tkadletz et al. [7] and the recently published paper by Moreno et al., which conducted *operando* high energy X-ray diffraction of PVD (Al,Ti)N coatings during high-speed metal cutting. Their study demonstrated temperatures higher than 727 °C along the tool edge and that the strain evolution varies at different positions in the coating due to both thermal and mechanical stresses. [26] Both studies utilize synchrotron X-ray diffraction to investigate the strain in the coating *in situ* during annealing or *operando* during cutting and showcase the importance of these types of measurements in order to understand the role residual stresses play in the performance of (Al,Ti)N coatings.

In this work, the effect of post-annealing after deposition was investigated for CVD (Al,Ti)N coatings deposited onto cemented carbide substrates. Possible improvements of the coating performance due to the post-annealing were evaluated with respect to residual stresses and thermal stability. *In situ* high energy synchrotron X-ray diffraction was used to study the phase evolution during heating to 1200 °C for both coatings. Peak fitting of selected (Al,Ti)N, TiN and hAlN peaks was used to investigate the decomposition reactions and calculate the temperature-dependent residual stress in the (Al,Ti)N phase. The observations were supported by electron microscopy of the coatings before and after the *in situ* heating cycle. The thermal stability was found to be relatively insensitive to post-annealing, as the spinodal decomposition and transformation reactions were not significantly altered and the final decomposition temperature was unaffected. Mechanisms governing the residual stress evolution in the (Al,Ti)N coatings are also discussed, where the stresses heavily depend on the degree of hAlN formation in the coatings.

2. Experimental

(Al,Ti)N coatings were deposited onto cemented carbide inserts (94 wt% WC, 6 wt% Co) with SNMA120412 geometry in an industrial low pressure CVD process. Prior to coating deposition, the inserts were ground on the top rake face using a grinding wheel of D25 grain size and cleaned. A TiN adhesion layer of approximately 1 μm thickness was deposited from $TiCl_4$, N_2 and H_2 as precursor and carrier gases at 850 °C and pressures below 150 mbar. The (Al,Ti)N coatings were deposited using $TiCl_4$, $AlCl_3$ and NH_3 as precursor and carrier gases at a temperature between 700 °C and 750 °C and a pressure below 25 mbar. The (Al,Ti)N-layer had an approximate thickness of 6 μm and overall composition of $Al_{0.85}Ti_{0.15}N$ determined by energy dispersive X-ray spectroscopy (EDS). To investigate the effect of post-annealing on the thermal stability of the coatings, one sample was isothermally annealed in Ar atmosphere at 850 °C for 3 h after coating deposition. The annealing was performed in a vacuum tube furnace slightly above atmospheric pressure to avoid surface oxidation. Prior to heating, 3 cycles of evacuation and venting with Ar were done at room temperature, and another cycle at 100 °C to evacuate adherent moisture in the system. The heating rate was set to 13.75 °C/min. After switching off heating, the upper part of the furnace was swung open to achieve a maximum cooling rate. The inserts were cut in half using a diamond cut-off wheel by a Struers Accutom equipment prior to the *in situ* synchrotron measurements.

In situ high energy grazing incidence transmission X-ray diffraction experiments were conducted at the P07 beamline at Petra III, DESY (Hamburg, Germany). The experimental setup is illustrated in Fig. 1. A 400 × 100 μm^2 rectangular beam with an energy of 103.8 keV (λ = 0.119450 Å) was used. Full ring diffractograms were recorded using a Perkin Elmer XRD 1621 flat panel detector. A LaB_6 standard powder was used for calibration. Each frame was an average of 40 images with 0.1 s exposure (4 s effective exposure time), where a corresponding dark frame was subtracted from each recorded frame. The samples were placed with the rake face parallel to the beam in a dilatometer setup (DIL 805 dilatometer), where they were held in place by Al_2O_3 rods and heated by induction in vacuum (Fig. 1). The thermocouple was attached to the samples on the WC substrate exposed by the cutting of the inserts (Fig. 1), which could lead to an underestimation of the actual temperatures in the coating, due to temperature gradients through the sample. The incidence angle was set by manually tilting the samples a few degrees around the y-axis (ω in Fig. 1) relative to the incoming beam, to increase the signal from the coating relative to the substrate. The heating cycle consisted of a fast heating step using 50 °C/min up to 600 °C, followed by a slower heating step using 25 °C/min in the temperature range where the decomposition reactions are expected to occur and up to 1200 °C. The samples were held at the maximum temperature for 10 min, before cooling with an average rate of 200 °C/min. The temperature profiles are shown in Fig. 3, Fig. 6, and Fig. 7.

Data processing and analysis was performed using Jupyter Notebooks utilizing the pyFAI python package [27] and scripts based on the *xrdfit* python package [28]. Due to shadows on the detector from absorption and scattering of the sample blocking the beam, only the top 160° of the diffractogram could be used (Fig. 1). An integration of the full 160° range was done for each frame for following the phase evolution with maximum temperature resolution. For stress calculations the 2D diffraction images were also integrated with an azimuthal slicing of 10° ("caked"). To increase the signal-to-noise ratio in the caked data used for residual stress calculations, 5 frames were averaged stepwise, giving an effective temperature resolution (*i.e.* change in temperature between the averaged frames) of *ca.* 41 °C/frame during the fast heating segment, *ca.* 19 °C/frame for the slow heating segment, and *ca.* 91 °C/frame during cooling. Peak fitting was done using a Pseudo-Voigt function for all the recorded frames during heating for both the caked and fully integrated data, where the limits for each peak were functions of temperature to account for thermal expansion. The *d*-spacings from the peak fitting of the caked data was used to calculate residual stresses in the different phases following the procedure outlined in Meindlhumer et al. [24], where the slope of the d-sin$^2\gamma$ curve

$$m = \frac{\partial d^{hkl}(T)}{\partial sin^2\gamma} = \sigma_r(T)\frac{1}{2}s_2^{hkl}(T)d_0^{hkl}(T) \quad (1)$$

is related to the equibiaxial in-plane residual stress (σ_r), the X-ray elastic constant ($\frac{1}{2}s_2^{hkl}$) and the strain-free lattice parameter (d_0^{hkl}) for the respective reflection. Note that Eq. (1) correspond to the standard sin$^2\Psi$-approach to residual stress determination, with $\Psi \sim \gamma$. Errors due to this approximation are negligible as the diffraction angles are small. The use of Eq. (1) is based on the assumption of an equibiaxial stress state, motivated by the small coating thickness. Errors for the d-spacings were used to weight the data in the line fit to remove uncertain data points. The temperature-dependent (assumed isotropic) X-ray elastic constants for each {hkl}-reflection for (Al,Ti)N were calculated by DECcalc [29] based on temperature and composition-dependent single crystal elastic constants C_{ij} from Shulumba et al. [30]

The microstructure of the as-deposited and post-annealed (Al,Ti)N coatings were imaged both before and after the *in situ* synchrotron experiments. The surface morphology of the coatings was characterized in a Zeiss Leo Ultra 55 Gemini field emission gun scanning electron microscope (SEM) using the secondary electron detector. Cross-sections of the coatings were studied by preparing thin foils from the sides/edges of the inserts using an FEI Versa 3D focused ion beam SEM (FIB-SEM) with an Omniprobe micromanipulator. Imaging of the cross-sections was performed in an FEI Titan 80–300 aberration-corrected transmission electron microscope (TEM). The TEM instrument was operated in the scanning mode (STEM) at 300 kV and equipped with a bright field (BF) detector, a high angle annular dark-field (HAADF) detector and an Oxford X-ray EDS detector.

3. Results

3.1. *In situ heating of (Al,Ti)N coatings*

The microstructure of the as-deposited and post-annealed (Al,Ti)N coatings was investigated both by SEM and STEM (Fig. 2). Images were acquired for equivalent samples in the as-deposited and post-annealed state before they underwent the *in situ* heating cycle during the synchrotron measurements. The BF STEM images of the as-deposited and post-annealed coating (Fig. 2(a) and (b), respectively) demonstrate elongated grains that extend through the whole coating layer. The insertions show an SEM image of the surface morphology of the coating, where the characteristic pyramidal grains can be seen in both coatings. Post-annealing did not significantly alter the microstructure of the coating, compared to the as-deposited coating, with one exception: hAlN grains at the (Al,Ti)N grain boundaries. Small amounts of tiny hAlN grains can be seen in the as-deposited coating, but these were hard to image, while the phase fraction and grain size of hAlN on the (Al,Ti)N grain boundaries significantly increased after post-annealing (Fig. S1 in the supplementary information). Fig. 2(c) shows one (Al,Ti)N grain in the post-annealed coating tilted to the zone axis, where the presence of hAlN grains along the (Al,Ti)N grain boundary is clearly visible. A high-resolution STEM image of one of the hAlN grains (Fig. 2(d)) was used to

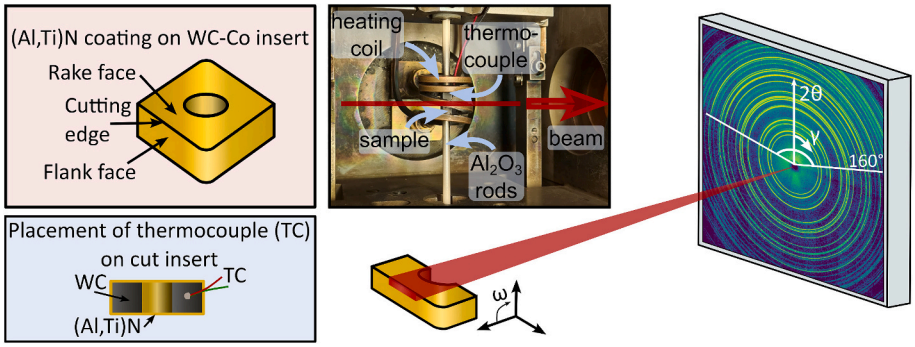

Fig. 1. Overview of the experimental setup at the P07 beamline at DESY (Hamburg, Germany) showing the sample orientation relative to the incoming beam and the coordinate system for the azimuthal division of data relative to the diffraction rings is indicated on the detector. The sample geometry, placement of the thermocouple and the inside of the dilatometer used in the experiment are also illustrated.

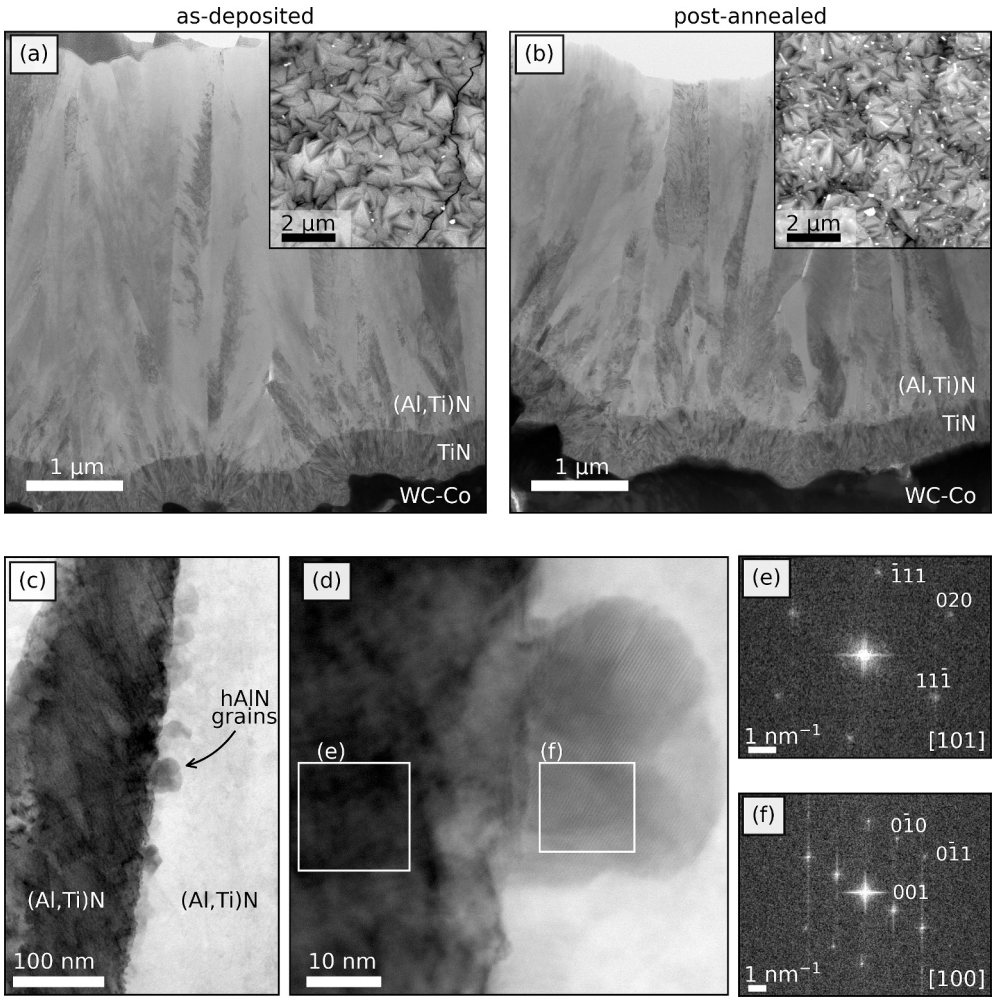

Fig. 2. BF STEM images of the microstructure of the (a) as-deposited and (b) post-annealed coating, before the *in situ* heating cycle, taken on the side of the insert that was not finely ground (bottom rake face). The insertions are secondary electron SEM images showing pyramidal microstructure of the coating surfaces. The post-annealing resulted in hAlN formation at the grain boundaries, exemplified by the BF STEM images in (c) and (d). Fast Fourier transformation (FFT) of the regions indicated in subfigure (d), demonstrating the crystal structure of (e) (Al,Ti)N and (f) hAlN along the [101] and [100] zone-axis, respectively.

confirm the crystal structure of the (Al,Ti)N and hAlN grains. Fast Fourier transformations (FFTs) of different regions in the grains are shown in Fig. 2(e) and (f), demonstrating the topotaxial formation of hAlN on the grain boundaries of the (Al,Ti)N grains where the c-axis of hAlN phase is oriented along the ⟨111⟩ – direction of the (Al,Ti)N phase, in agreement with previously reported orientation relationships. [17]

Synchrotron XRD patterns were continuously recorded during the heating cycle to 1200 °C for both as-deposited and post-annealed (Al,Ti)N coatings. The resulting 2D surface plots are presented in Fig. 3(a) and (b), respectively, where the first part of the heating cycle is cut, as no changes occurred below 700 °C. The full dataset is shown in Fig. S2 in the supplementary information. The corresponding temperature profile for the diffraction patterns is shown in Fig. 3(c). Diffractograms at room temperature before the *in situ* heating cycle and at the maximum temperature (red dashed line in the 2D surface plots) for both samples are included in Fig. 3(d) and (e). At room temperature, prior to the heating cycle, the diffraction patterns (Fig. 3(d) and (e)) exhibit peaks from the cubic (Al,Ti)N coating, the cubic TiN adhesion layer and the WC-Co substrate. At elevated temperatures, distinct broad peaks attributed to hAlN appear in the 2D surface plots (Fig. 3(a) and (b)), with neglectable diffraction signal prior to the *in situ* heating cycle. Moreover, there is an abrupt change in the diffraction patterns of both the as-deposited and post-annealed coatings around 1070 °C, where the (Al,Ti)N peaks disappear (indicated by a black dotted line in Fig. 3), leaving only peaks from TiN and hAlN in the coating, which implies that the spinodal decomposition and transformation reactions in the bulk of the coating occurs quickly above a certain temperature threshold. It's noteworthy that the diffraction peaks from the hAlN phase only appears in the diffractograms around the temperature where the (Al,Ti)N phase disappears, approximately at 1070 °C, while small hAlN precipitates at the (Al,Ti)N grain boundaries have been observed by STEM in this work and previously by TEM by Bäcke et al. [17], especially for post-annealed coatings. This means that the amount of grain boundary hAlN formed during the post-annealing is below the limit for a detectable signal in the diffractograms.

Peaks attributed to the cemented carbide substrate, namely WC [31], hexagonal Co_3W (PDF Card 01–071-7505) and cubic Co_6W_6C [32], were identified based on their *d*-spacings. The peaks at 3.030 $Å^{-1}$ and 3.506 $Å^{-1}$ are presumed to originate from cubic Co [33] in the substrate binder phase. At elevated temperature, tungsten and carbon dissolve into the Co-phase, which results in peak splitting and the notable shift in *d*-spacing, which reverts back to a single Co-phase during cooling though WC precipitation. The peaks from the substrate are indicated as "WC" in black and "sub." in purple in Fig. 3, referring to the main WC phase and the other phases (Co_3W, Co_6W_6C, Co), respectively. The {400} and {333} peaks of Co_6W_6C partially overlap with the {100} hAlN and {200} TiN peaks, respectively, and the {111} of the presumed Co-phase partially overlap with the {200} (Al,Ti)N peaks. Consequently, these

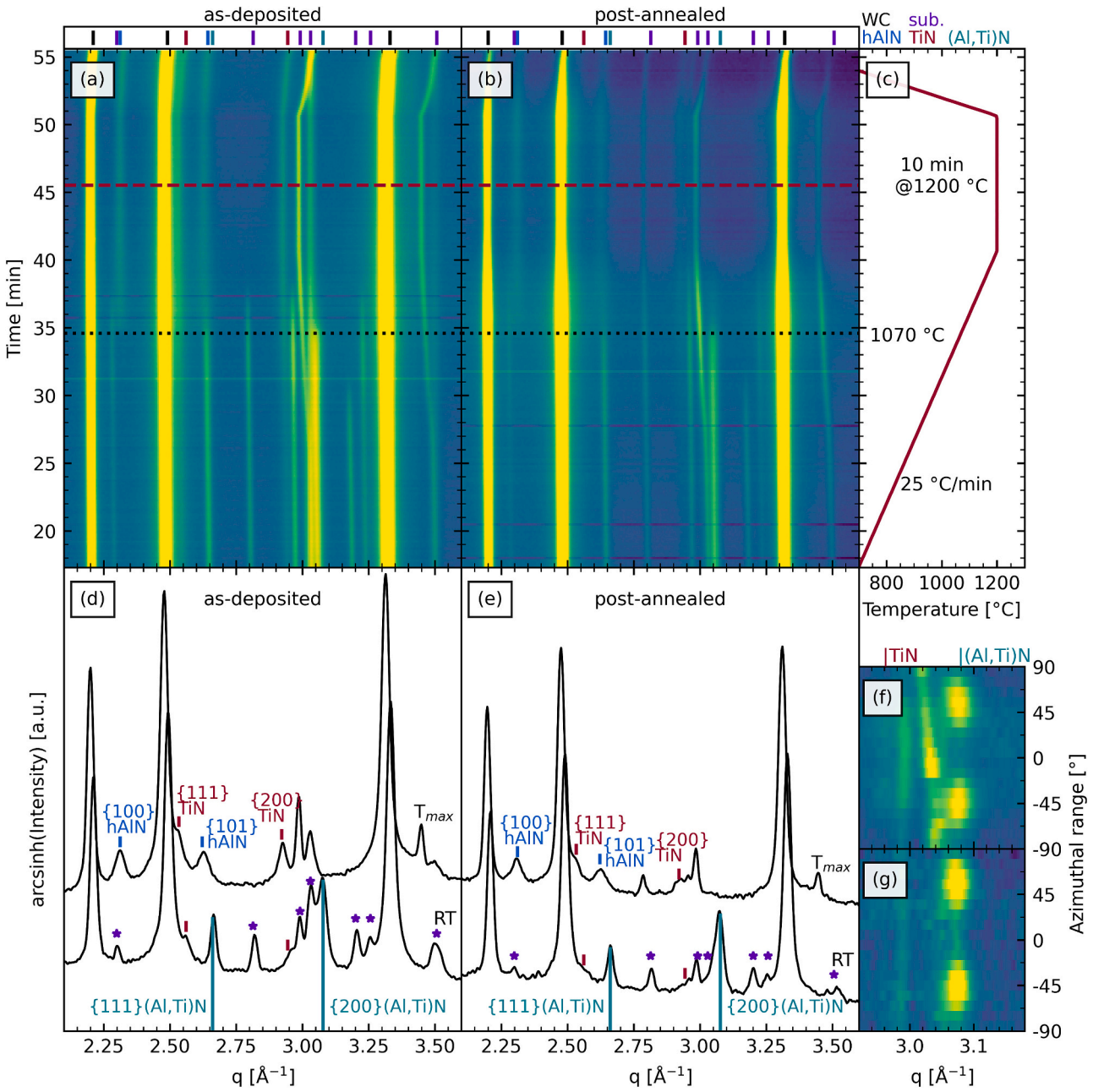

Fig. 3. 2D surface plots of the full 160° integrated diffractograms recorded during the heating cycle for (a) the as-deposited and (b) the post-annealed (Al,Ti)N coatings. Intensities are on an arcsinh(I)-scale. Peaks corresponding to hAlN, TiN, (Al,Ti)N and peaks from the substrate; WC and other phases (Co_3W, Co_6W_6C and Co, denoted "sub.") and are indicated in the top panel with their room temperature values. Horizontal lines are intensity changes as a result of sample movements during heating. (c) Time-Temperature profile of the *in situ* heating cycle for both samples. Diffractograms at room temperature before the heating cycle and at the maximum temperature (red dashed line in 2D surface plots at 46 min) are shown for (d) the as-deposited and (e) the post-annealed sample, where the indices of the coating related peaks are also indicated. The substrate phases (Co_3W, Co_6W_6C and Co) are marked by asterisks in the room temperature diffraction pattern. The room temperature 2D diffractograms before the heating cycle in the q-range that contain the {200} TiN and the {200} (Al,Ti)N peaks are shown in (f) and (g) for the as-deposited and post-annealed samples, respectively, illustrating the textured nature of the (Al,Ti)N coating. (For interpretation of the references to colour in this figure legend, the reader is referred to the web version of this article.)

peaks were also included in the peak fitting process. Despite the presence of substrate-related diffraction peaks, these are not the central focus of our analysis and are not elaborated upon further. The most intense diffraction lines in Fig. 3 are from the WC substrate, as difficulties with sample alignment resulted in large intensity differences. All diffractograms are therefore plotted with an arcsinh-scaling of the intensity to enhance the visibility of the weak coating peaks, while not amplifying the noise in the background too much.

The (Al,Ti)N coatings have a {111} preferred orientation, which can be seen by the azimuthal dependence of the intensity of the diffraction rings in Fig. 3(f) and (g) for the as-deposited and the post-annealed coating, respectively. The intense arc sections on the {200} rings at positions in agreement with the expected ±54.7° reflections for {111} preferred orientation (and the arc section at 0° on the {111} ring shown in Fig. S1 in the Supplementary Information), serve as clear indicators. The positions of the arcs are similar for both samples, as texture is not expected to change due to post-annealing. Additionally, the signal from the TiN adhesion layer is only seen as a weak diffraction line showing no

intensity variation with the azimuthal angle, implying a random texture.

The microstructure of the as-deposited and post-annealed (Al,Ti)N coatings after the *in situ* synchrotron heating cycle are shown in Fig. 4. The coatings are completely decomposed and consist of hAlN and TiN. In certain areas, the remains of the initial structure can still be seen (bottom insertions), as TiN particles (dark spots) that formed according to the original lamella structure. This is in accordance with the synchrotron measurements demonstrating only diffraction peaks from hAlN and TiN after the heating cycle (Fig. 3). The pyramidal surface morphology (top insertions) was still intact after decomposition.

3.2. Peak fitting and stress calculations

The phase evolution was examined more in detail by fitting peaks for the (Al,Ti)N, TiN and hAlN phases for the fully integrated diffractograms. Residual stress for the (Al,Ti)N peaks were calculated based on the caked diffractograms from fitting a straight line to the d-$\sin^2\gamma$-curves, like the one shown in Fig. 5(a), and entering the values for the slope m and d_0 in Eq. (1). The data points were weighted based on the errors from the peak fitting (error bars), to improve the accuracy of the stress calculation. Selected representative peak fits are illustrated in Fig. 5(b)-(g) for different azimuthal angles and temperatures for the {200} TiN and {200} (Al,Ti)N peaks, which are overlapping with peaks from the substrate. The peak fitting is complicated due to the (Al,Ti)N {111} texture, making the intensity and peak overlap with substrate peaks a function of both the azimuthal angle (Fig. 5(b)-(d)), and temperature (Fig. 5(e)-(g)) as peak widths, intensities and positions will shift at elevated temperatures. The temperature-dependent peak limits are indicated as vertical dashed lines, set to compensate both for the changes in temperature, but also to make sure the right peak is fitted when the degree of peak overlap change as a function of the azimuthal angle. The amplitudes (area under the peaks) from the peak fitting were normalized based on the room temperature value for the (Al,Ti)N peaks, while the TiN and hAlN peaks were normalized based on the room temperature value after annealing. Consequently, the intensity ratios are not representative of phase fractions, but they allow qualitative analysis of changes in the amount of the different phases. All peaks were also corrected according to the background intensity.

The results of the fits of the {110} hAlN, {220} TiN and {222} (Al,Ti)N peaks are displayed in Fig. 6, while the fits of the {100}, {200} and {222} (Al,Ti)N peaks are compared in Fig. 7. The black dots on the 2D surface plots indicate the peak positions determined by the peak fitting, while the corresponding normalized amplitudes of the peaks as a function of temperature are displayed to the right. The full temperature profiles of the samples are shown on the left. The {110} hAlN, {220} TiN and {222} (Al,Ti)N peaks were selected for visualisation of the phase evolution as there is no overlap with other peaks, despite the lower intensity compared to lower index reflections. At low temperatures, cubic TiN (from the adhesion layer), (Al,Ti)N and substrate phases are present in both the as-deposited and post-annealed sample. Upon heating to 600 °C, the amplitude of the (Al,Ti)N and TiN peaks decreases for both samples (Fig. 6(d) and (h) for as-deposited and post-annealed coating, respectively), which is likely an effect of the increasing Debye-Waller factor (intensity decay due to thermal vibrations), rather than an indication of any reactions, especially considering the corresponding increase in peak amplitudes occurring during cooling of the samples. Moreover, the Debye-Waller factor gives a stronger effect for higher index reflections, which fits with the behaviour seen in both the as-deposited and post-annealed coating (Fig. 7(e) and (k), respectively). A rapid decrease in (Al,Ti)N amplitudes is observed in the temperature range from around 900 °C to approximately 1070 °C in both coatings (Fig. 6 and Fig. 7). The latter temperature is assumed to correspond to the complete transformation of (Al,Ti)N. The amplitude of the TiN peaks for the two samples is relatively stable until there is a rapid increase from around 900 °C until the coating is fully transformed. The increase in the TiN intensity could be interpreted as the onset of spinodal decomposition of (Al,Ti)N to TiN and metastable cubic AlN. This would thus be expected to be accompanied by the appearance of shoulders on the (Al,Ti)N peaks corresponding to cubic AlN. [17] No such shoulder was not observable in the data presented in this work, most likely due to the weak intensity from the coating peaks relative to the substrate signal. However, it could also be affected by the high Al-content in (Al,Ti)N (Al = 0.85), since the d-spacing of the cubic (Al,Ti)N and the cubic AlN phase are close, it would be hard to differentiate between those two phases with the peak resolution in this work, especially taking the shift due to thermal expansion into account. No hAlN phase was observed in the diffractograms below the temperature for complete (Al,Ti)N transformation, while above this temperature, the amplitude of the hAlN peak increases, and this peak also becomes visible in the diffractograms (Fig. 6(b) and (f)). This suggests that while hAlN have been reported to form along grain boundaries at lower temperatures [7,17,18], this process is too slow to give detectable amounts of hAlN (at the current

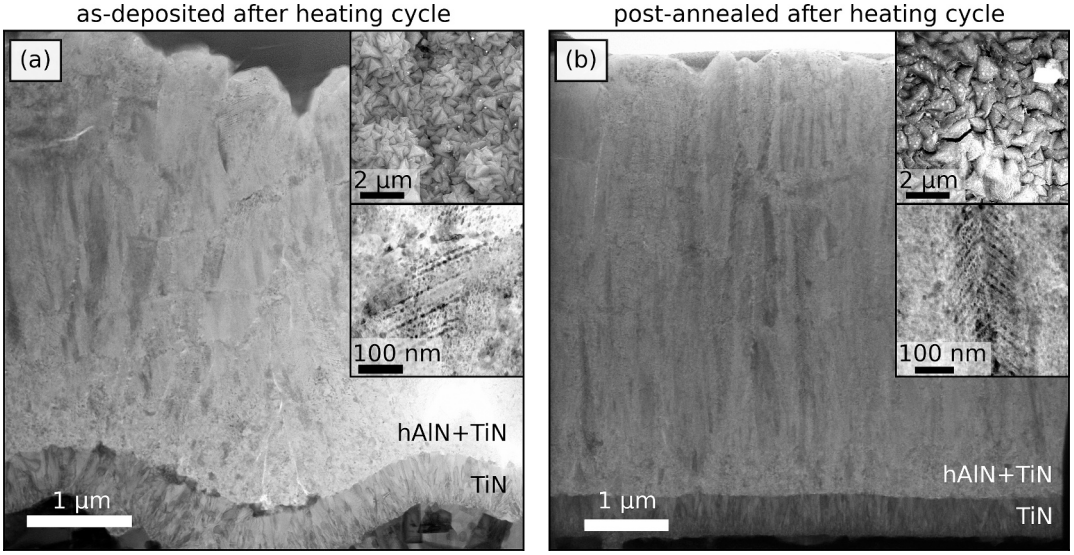

Fig. 4. BF STEM images of the fully decomposed microstructure of the (a) as-deposited and (b) post-annealed coating, after the *in situ* heating cycle on the unground (bottom rake face) and the ground (top rake face) side of the inserts, respectively. The top insertions are secondary electron SEM images showing the pyramidal microstructure of the coating surface. The bottom insertions are BF STEM images showing remains from the original lamellar microstructure of the coatings.

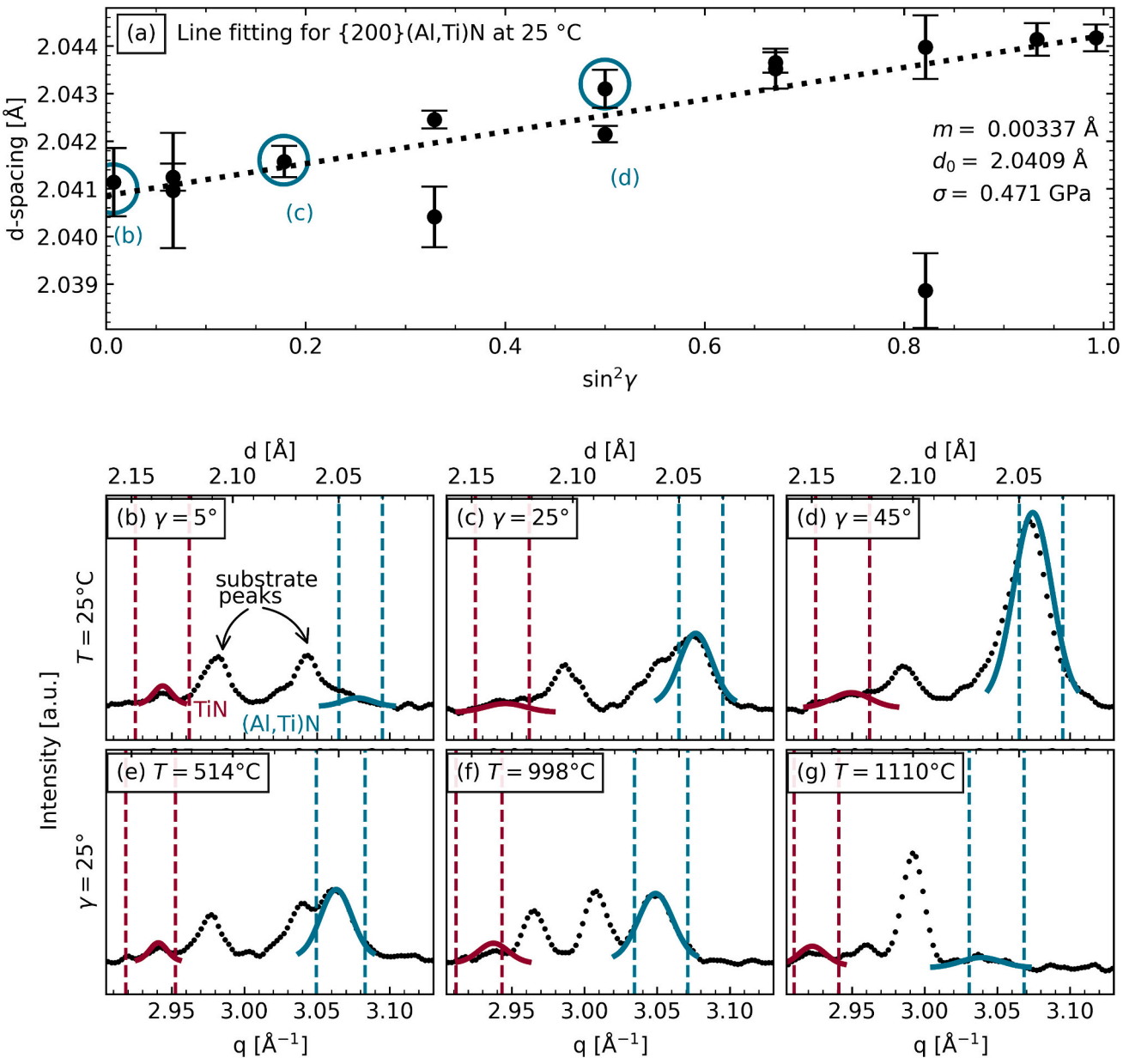

Fig. 5. Typical results from the peak fitting and stress calculations. (a) Position of the peaks (d-spacing) plotted as a function of the azimuthal angle (γ), and the corresponding weighted line fit for the {200} (Al,Ti)N peak. The values from the fits in subfigure (b)-(d) are indicated. (b)-(d) shows peak fitting of the {200} peaks of TiN and (Al,Ti)N from the first frame of the as-deposited sample at room temperature, before the *in situ* synchrotron heating cycle. Due to the textured nature of the (Al,Ti)N coating, the intensity varies with the azimuthal angle (γ). The overlap with substrate peaks, which also show some variation with the azimuthal angle, meant that the peak fitting was non-trivial. (e)-(g) The TiN, (Al,Ti)N and substrate peaks also showed changes in intensity, peak width and position as a function of temperature, further complicating the peak fitting process. The dashed lines are the borders of the peaks, which were varied as a function of temperature.

heating rate) before the complete transformation occurs around 1070 °C. [17] The abrupt transformation of the (Al,Ti)N coating is also evident from the {111} and {200} (Al,Ti)N peaks, presented in Fig. 7, along with the {222} peak, for both the as-deposited and post-annealed coating. This demonstrates that even though the intensity from the {222} (Al,Ti)N peak is weaker compared to the lower index peaks, the observed behaviour is representative for reactions in the coating, as all the fitted (Al,Ti)N peaks display similar behaviour, for both samples. However, the {111} (Al,Ti)N peak (Fig. 7(b) and (g)) overlap in position with the {101} hAlN peak at elevated temperature, so the amplitude and the position for the {111} (Al,Ti)N peak are indicated below 1070 °C. All the (Al,Ti)N peaks exhibit a sharp decrease in the peak amplitude before the coating is fully transformed, and the amplitude of the {200} and {222} peaks stabilize close to zero afterwards for both samples. A noteworthy feature in the 2D surface plots in both Fig. 6 and Fig. 7, for both the as-deposited and post-annealed sample, is the change in background intensity (and peak intensities) during heat and cooling. The experimental setup did not facilitate adjusting for thermal expansion or movements due to temperature change, which resulted in apparent intensity changes that are solely due to sample movement and not to changes in the coating, which made it necessary to normalize the amplitudes from the peak fitting to the background.

From the peak fitting of the (Al,Ti)N peaks, residual stresses were calculated, and a symmetric moving average is presented to make the trends more visible and reduce the noise. Fig. 8 displays the residual stress for both the as-deposited and post-annealed sample, demonstrating a very cohesive stress evolution obtained from the {111} and {200} peaks. The residual stress of the {222} (Al,Ti)N peak is not

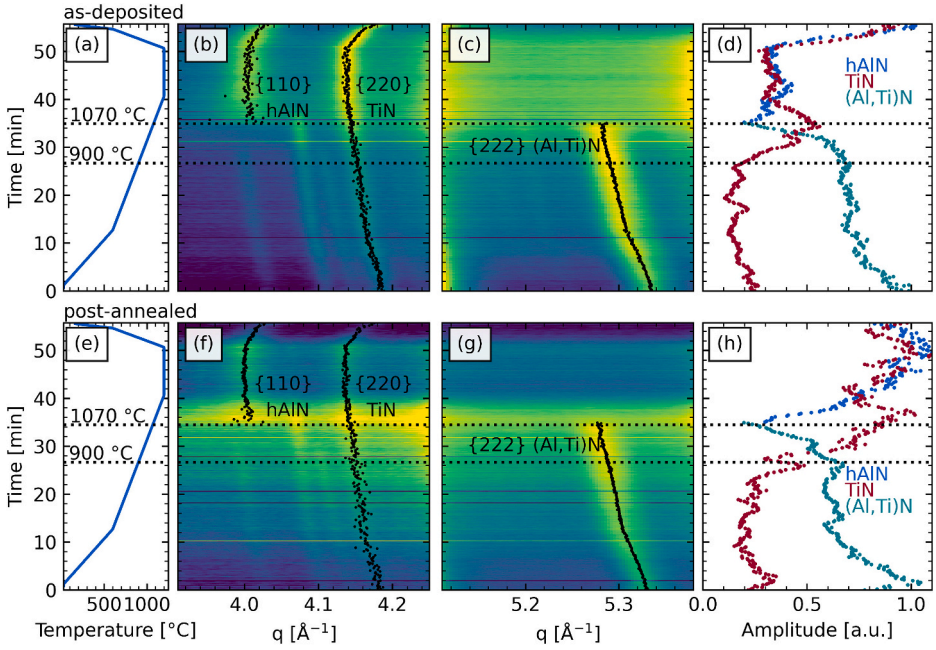

Fig. 6. (a) and (e) Time-temperature profiles of the *in situ* heating cycle for the as-deposited and post-annealed (Al,Ti)N coating. 2D surface plots of the integrated diffractograms recorded during the synchrotron heating cycle for (b) and (f) the {110} hAlN and {220} TiN peaks and (c) and (g) the {222} (Al,Ti)N peak, where the position from the peak fitting is indicated with black dots. (d) and (h) Normalized amplitudes from the peak fitting. The black dashed horizontal lines are guides to the eye and indicate the start and end temperatures for the coating decomposition.

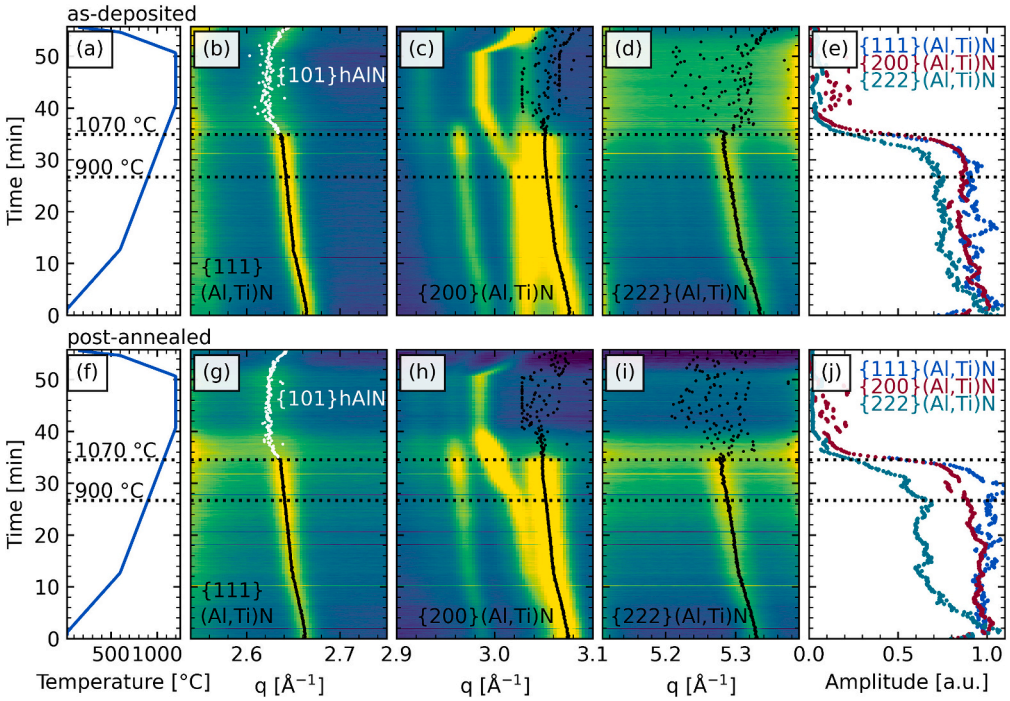

Fig. 7. (a) and (g) Time-temperature profiles of the *in situ* annealing for the as-deposited and post-annealed (Al,Ti)N coating, respectively. 2D surface plots of the integrated diffractograms recorded during the synchrotron heating cycle for (b) and (h) the {111} (Al,Ti)N peak, (c) and (i) the {200} (Al,Ti)N peak and (d) and (j) the {222} (Al,Ti)N peak, where the position from the peak fitting is indicated with black dots for (Al,Ti)N and white in the case of the {101} hAlN peak overlapping with the {111} (Al,Ti)N. (e) and(k) Normalized amplitudes from the peak fitting. The black dashed horizontal lines are guides to the eye and indicate the start and end temperatures for the decomposition.

included, as the low intensity of this peak makes the signal-to-noise ratio too high after caking to produce reliable results. The residual stress is tensile in both samples at room temperature, but the post-annealing has resulted in a decrease of the room temperature residual stress, from 0.40 to 0.27 GPa for the {111} peak and 0.43 to 0.10 GPa for the {200} peak. The expected average macroscopic stress evolution solely due to mismatch in coefficient of thermal expansion (CTE) between (Al,Ti)N and WC are indicated as a grey dashed lines in Fig. 8, and calculated by fitting a line with the stress values for the {200} peak and fixing the slope to the one given by CTE mismatch [34] and the *E*-modulus for (Al,

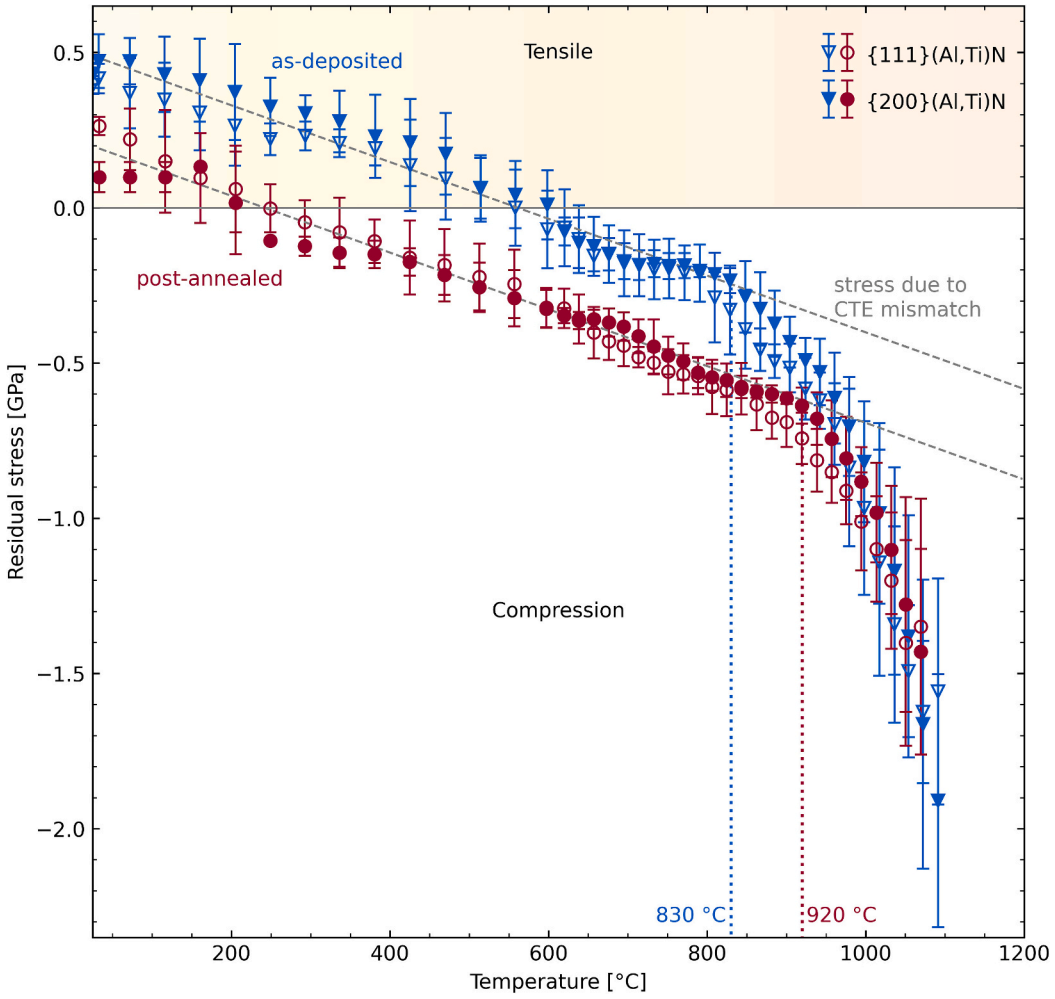

Fig. 8. Symmetric moving average of the residual stress in both the as-deposited and post-annealed (Al,Ti)N coatings for the {111} and {200} peaks. The standard deviation from the moving average calculation is represented by error bars. The macroscopic stress due to mismatch of coefficient of thermal expansion (CTE) is illustrated by the grey dashed lines based adjusted to overlap with the linear region of the {200} peak for both coatings. The blue and red dashed lines indicate the suggested onset of the decomposition. (For interpretation of the references to colour in this figure legend, the reader is referred to the web version of this article.)

Ti)N [35]. Notably, both samples seem to align with the expected thermal stress up until around 900 °C, above which the residual stresses of both samples deviate from the expected trend, and the difference between the two samples gradually diminish, ultimately converging at the same level of compressive stress before the coating is fully transformed. The deviation from the expected trend occurs at a lower temperature in the as-deposited coating (*ca.* 830 °C) than the post-annealed coating (*ca.* 920 °C), suggesting that the onset of the decomposition was slightly delayed by the post-annealing. Due to the governing influence of the CTE mismatch on the residual stress evolution in both samples, the reduction observed at room temperature due to post-annealing was retained even above the post-annealing temperature. Furthermore, the decrease in room temperature residual stress also leads to a reduction in the temperature necessary for achieving compressive stresses in the coating. This transition occurs at approximately 560 °C for the as-deposited but is reduced to around 240 °C after post-annealing.

4. Discussion

4.1. Spinodal decomposition and transformation in CVD (Al,Ti)N coatings

Microstructural investigations revealed hAlN particles at the (Al,Ti)N grain boundaries for both the as-deposited and the post-annealed coating before the synchrotron measurements (Fig. 2). Although in the case of the as-deposited coating, the size of the hAlN grains was small, making them hard to image. After post-annealing at 850 °C for 3 h, there was a significant increase in the phase fraction and grain size of hAlN along the (Al,Ti)N grain boundaries. This is in line with previous microstructural investigations. [17] The *in situ* X-ray diffraction patterns of both the as-deposited and the post-annealed (Al,Ti)N coating in this work showed that the coatings follow the decomposition pathway outlined in previous studies. [7,17,18] Only peaks corresponding to (Al,Ti)N, TiN and the substrate were observed in the diffraction patterns (Fig. 3, Fig. 6, Fig. 7) prior to the *in situ* heat cycle. No peaks corresponding to hAlN appeared in the X-ray diffraction patterns, likely due to limited amounts of this phase in combination with the challenging sample alignment and the resulting weak peak intensities form the coating phases.

Upon heating from room temperature, there was no significant change in the diffraction peaks of the coating phases below around 900 °C (Fig. 6), but above 900 °C the amplitudes of the (Al,Ti)N peaks start to decrease, while the amplitudes of the TiN peaks start to increase. Based on previous reports, this decrease in the amplitude of the (Al,Ti)N peaks coupled with the increase in the amplitude of the TiN peak is interpreted as due to the spinodal decomposition reaction

$$c(Al,Ti)N \rightarrow cAlN + cTiN \quad (2)$$

even though the corresponding cubic AlN phase is not observed in the diffraction patterns (Fig. 7). Despite the presence of hAlN along the grain boundaries in both the as-deposited and post-annealed (Al,Ti)N coatings, diffraction peaks of hAlN only appear in the diffraction patterns (Fig. 6) above approximately 1070 °C, where the (Al,Ti)N peaks are no longer visible in the diffraction patterns (Fig. 7). This temperature corresponds to the complete transformation of the coating, where hAlN forms either by transformation of preceding spinodal decomposition through the reaction

$$cAlN \rightarrow hAlN \tag{3}$$

or by transformation from (Al,Ti)N directly

$$c(Al,Ti)N \rightarrow hAlN + cTiN \tag{4}$$

Previous work show that the reactions initiate at the grain boundaries and at the coating surface, but that at temperatures below 1000 °C these reactions are slow and self-limiting due to the volume expansion associated with the formation of hexagonal phase at the grain boundaries. [17] These observations fit well with the limited changes in the diffraction peaks observed in this work, with onset of decomposition occurring around 900 °C and complete transformation after reaching 1070 °C. Further, this work demonstrates no significant effect of the post-annealing on the thermal stability of the (Al,Ti)N coatings. While there appears to be an increase in the onset temperature of the decomposition, this aspect will be discussed further in connection to the residual stress evolution below.

4.2. *Mechanisms governing the temperature dependent residual stresses in (Al,Ti)N CVD coatings*

The temperature-dependent residual stress evolution for the {111} and {200} (Al,Ti)N peaks for the as-deposited and post-annealed coating (Fig. 8) shared some similarities. Both the as-deposited and post-annealed coating initially followed a linear trend. However, in the temperature range of 800–950 °C, the coatings deviate from the expected thermal stress. Moreover, post-annealing reduced the room temperature tensile stress in the (Al,Ti)N coating and led to an increase in the onset temperature for the accelerated development of compressive stress from 830 °C in the as-deposited coating to 920 °C in the post-annealed. This observed behaviour can be understood by considering two mechanisms contributing to the stress state of the (Al,Ti)N phase; CTE mismatch and growth of hAlN. These mechanisms are illustrated in Fig. 9, along with the moving average of the calculated residual stress for the {200} (Al,Ti)N peak in both the as-deposited and post-annealed coating.

Since the thermal expansion coefficient for the WC-Co substrate is smaller than that of the (Al,Ti)N coating, compressive stresses will start to develop in the coating upon heating from room temperature, as a linear function of the temperature (grey dashed lines in Fig. 8 and Fig. 9). This is exactly what is observed at low to intermediate temperatures, and if no other mechanism contributed to the residual stress state in the coating, post-annealing would not result in a change in residual stress. It is well documented in the literature and observed in this work

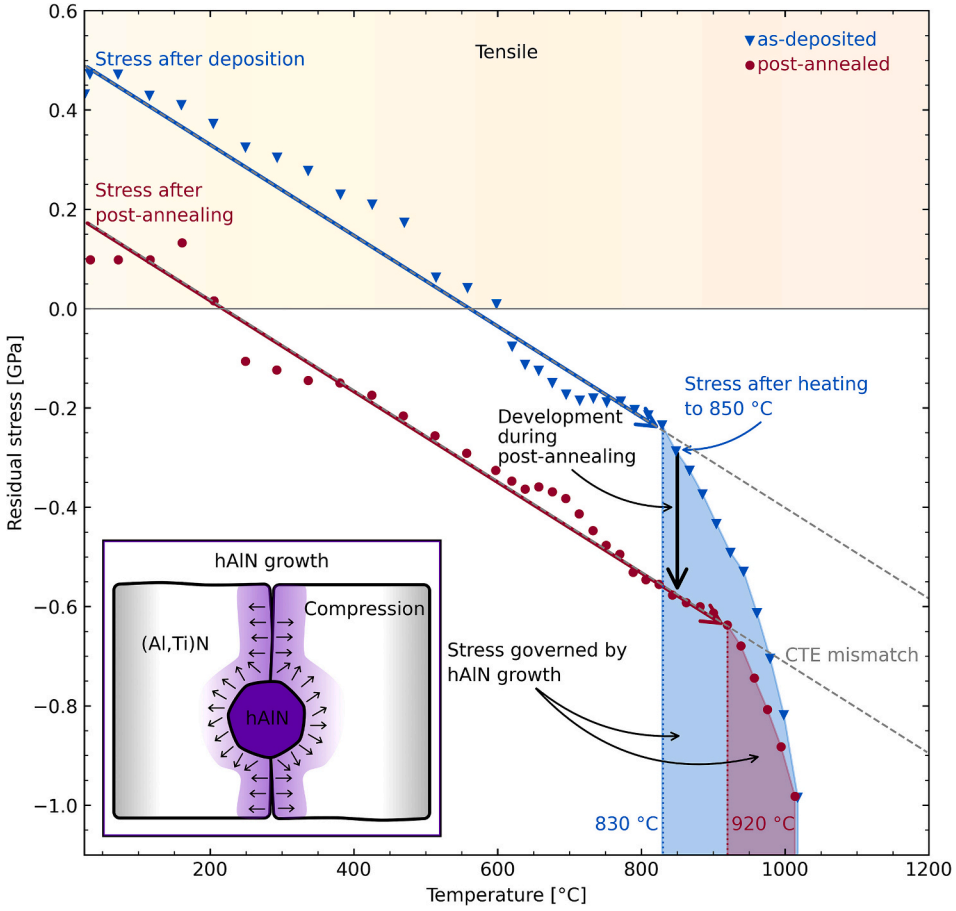

Fig. 9. Schematic overview of the mechanisms governing the temperature dependent stress development of (Al,Ti)N coatings. The data points are the moving average of the calculated residual stress for the {200} (Al,Ti)N peaks from Fig. 8. The expected stress from CTE mismatch with the substrate is indicated as grey dashed lines. The shaded regions signify temperatures where the residual stress is a combination of the CTE mismatch stress and the stress from growth of hAlN on the (Al,Ti)N grain boundaries. The latter mechanism is illustrated in the insert. The proposed change in stress occurring during the post-annealing is indicated by a black arrow.

(Fig. 2), that hAlN forms at the (Al,Ti)N grain boundaries at low to intermediate temperatures (< 900 °C) relative to the temperature where the decomposition is complete. The transformation from cubic to hexagonal AlN is associated with a volume expansion of around 26% [36], which creates compressive stresses in the (Al,Ti)N grains. Therefore, above around 830 °C, the residual stress in the as-deposited coating is mainly governed by the stress due to growth of the hAlN phase and is no longer solely controlled by the CTE mismatch, resulting in the accelerated stress development illustrated in Fig. 9. Since the hAlN growth in the as-deposited coating starts around 830 °C, a significant increase in the phase fraction and grain size of hAlN phase occurs during the 3 h post-annealing at 850 °C. This growth gives a more compressive stress state in the coating. The residual stress is also governed by the CTE mismatch during cooling, following the same linear behaviour down to room temperature but starting from the new, more compressive, stress state at the end of the 850 °C hold time. This results in the reduced tensile stress observed in the post-annealed coating at room temperature. Upon heating of the post-annealed coating, the onset of the hAlN growth is increased from 830 °C to 920 °C due to a more compressive residual stress state in the coating from already formed hAlN grains at the (Al,Ti)N grain boundaries (Fig. 2). As for the as-deposited coating, upon heating the post-annealed coating to temperatures above the onset of hAlN growth, the residual stress in the coating rapidly decrease from a combination of CTE mismatch and compressive stress developing from the continued growth of hAlN on the (Al,Ti)N grain boundaries. The stress approaches −2 GPa in both the as-deposited and post-annealed coating as the growth of hAlN continues, until the coating is completely transformed around 1070 °C.

Bäcke et al. suggested that the phase transformations are influenced interchangeably by temperature and time, given the metastable nature of the (Al,Ti)N phase. [17] From a stress evolution perspective this implies that the stress developed during the 3 h post-annealing period is analogous to continuously heating to a higher temperature. From Fig. 9, it can be inferred that post-annealing at 850 °C for 3 h effectively results in the same stress level found after heating to approximately 950 °C during the *in situ* exposure. The mechanisms outlined above remain valid only when the transformation is confined to the grain boundaries, and no bulk transformation occurs.

The calculated tensile stress of 0.43 GPa for the {200} (Al,Ti)N peak in the as-deposited coating at room temperature is somewhat lower than the expected value of 0.62 GPa based on stress from CTE mismatch development during cooling from the deposition temperature. Furthermore, the temperature where zero stress is reached (around 560 °C), is lower than the deposition temperature (700–750 °C), which is where a stress-free state would be expected. Considering the error bars in Fig. 8, the difference could be due to the measurement technique or caused by the small amount of hAlN formed at the grain boundaries in the as-deposited coating (Fig. S1). Only the post-annealed coating showed significant amounts of grain boundary hAlN (Fig. 2), which is believed to be the reason for the considerably lower stress state, 0.10 GPa tensile stress for the {200} (Al,Ti)N peak. The calculated residual stress values in this work were notably lower than those reported by Tkadletz et al. for (Al,Ti)N coatings from low pressure CVD investigated by *in situ* synchrotron XRD, where a tensile stress around 1.45 GPa at room temperature was calculated from the obtained microscopic lattice strain. [7] However, the maximum compressive stress of approximately −2 GPa at 1000 °C reported by Tkadletz et al. [7] corresponds well with the maximum compressive stresses found in this work (Fig. 8) at the final transformation temperature. The discrepancy in the room temperature residual stress values calculated in this work and those reported by Tkadletz et al., could be due to sample processing, as the properties of CVD (Al,Ti)N coatings are known to be dependent on processing parameters such as deposition temperature and pressure, both of which are lower in the current work (700–750° and < 25 mbar) compared to that of Tkadletz et al. (790° and 45 mbar) [7]. Different experimental approaches for the stress measurements could also influence the obtained residuals tress values. It is important to note that the X-ray elastic constants used for the stress calculations in this work are based on single crystal elastic constants from simulations, which have not been experimentally verified. Further, the $\sin^2\Psi$-approach assumes a texture-free coating with equiaxed grains, while the (Al,Ti)N coatings in this work exhibit columnar grains and {111}-texture (Fig. 2). Thus, the reported values should be interpreted as trends, rather than exact numbers. Inaccurate X-ray elastic constants would affect the slopes of the stress-temperature curves (Fig. 8), but not the point of zero stress. Nonetheless, the agreement between the slopes of the stress curves at lower temperatures and the stress expected from CTE mismatch indicate that the reported trends are realistic. Moreover, in the current work, difficult alignment of the samples before the *in situ* synchrotron measurements did result in weak coating peaks and a strong diffracted signal from the substrate, which influenced the peak fitting. These errors should be in the same order of magnitude for each of the coatings, meaning that even if the exact values might not be accurate, the trends found should still be valid. Especially considering the linear trend in the residual stress found for both coatings at low to intermediate temperatures. Additionally, it is worth noting that the placement of the thermocouple on the substrate side of the samples (Fig. 1) may have resulted in measured temperatures that are lower than the actual temperature within the coating, owing to thermal gradients across the sample. However, given the consistency of our data with the cited literature and the coherence of observed trends and mechanisms, any such discrepancy in the temperature measurements is unlikely to affect the general validity of our findings.

These results suggest the potential to extrapolate values of the residual stress measured at room temperature to higher temperatures, up to the onset of the decomposition. This is significant, as coated inserts experience elevated temperatures during cutting and machining. [26] Lastly, this work emphasises the importance of utilizing *in situ* characterization tools, such as high energy synchrotron X-ray diffraction, for investigating the mechanisms governing the spinodal decomposition and transformation reactions in these hard coating systems. The advantage of tracking the evolution of the residual stress was demonstrated, and its importance for understanding how the performance and service time of (Al,Ti)N coatings can be improved. The methods outlined demonstrate the potential of using *in situ* or *operando* synchrotron diffraction for investigating other aspects of the (Al,Ti)N coatings, such as mechanical impact, effects of TiN top layers or other types of post-treatments such as dry or wet blasting and the role residual stresses and hAlN formation plays in relation to the performance.

5. Conclusion

The effect of post-annealing on thermal stability and residual stress of CVD (Al,Ti)N coatings on cemented carbide substrates was investigated for using *in situ* high energy synchrotron X-ray diffraction, supported by electron microscopy. Temperature-dependent residual stresses were calculated based on fitting of selected (Al,Ti)N peaks, while the spinodal decomposition and transformation reactions were monitored by peak fitting of selected (Al,Ti)N, TiN and hAlN peaks. The *in situ* synchrotron measurements revealed no significant difference in phase evolution and thermal stability between as-deposited and post-annealed (Al,Ti)N coatings. Both the onset of the spinodal decomposition and the bulk transformation occur at similar temperature in both coatings. The residual stresses in both coatings were governed by the stress from mismatch in coefficients of thermal expansion with the WC-Co substrate. Post-annealing reduced the tensile residual stress at room temperature due to the increased phase fraction and grain size of hAlN, which contributes to compressive stresses in the (Al,Ti)N coating. The growth of hAlN also delayed the onset of the decomposition from 830 °C to 920 °C. Therefore, post-annealing is expected to enhance the performance and service time of (Al,Ti)N coating, by the formation of limited amounts of hAlN on the (Al,Ti)N grain boundaries, which promotes a more desirable compressive stress state in the coating for the

same service temperature.

CRediT authorship contribution statement

Kristine Bakken: Writing – review & editing, Writing – original draft, Visualization, Investigation, Formal analysis. **Olof Bäcke:** Writing – review & editing, Project administration, Investigation, Funding acquisition. **Samik Roy Moulik:** Writing – review & editing, Investigation. **Andreas Stark:** Resources. **Thorsten Manns:** Writing – review & editing, Resources, Investigation, Conceptualization. **Dirk Stiens:** Writing – review & editing, Supervision, Resources, Project administration, Funding acquisition, Conceptualization. **Mats Halvarsson:** Writing – review & editing, Supervision, Project administration, Funding acquisition, Conceptualization. **Magnus Hörnqvist Colliander:** Writing – review & editing, Supervision, Project administration, Funding acquisition, Conceptualization.

Declaration of competing interest

The authors declare the following financial interests/personal relationships which may be considered as potential competing interests.

Dirk Stiens and Thorsten Manns are employees of Walter AG, a commercial cutting tool manufacturer. If there are other authors, they declare that they have no known competing financial interests or personal relationships that could have appeared to influence the work reported in this paper.

Data availability

Data will be made available on request.

Acknowledgement

The funding for this work was provided by VINNOVA (The Swedish Innovation Agency) through the project 2021-03825. We acknowledge DESY (Hamburg, Germany), a member of the Helmholtz Association HGF, for the provision of experimental facilities. Parts of this research were carried out at the P07 beamline at PETRA III, where beamtime was allocated for proposal I-20220502 EC. The assistance of Fredrik Lindberg during the synchrotron measurements is gratefully acknowledged. The Swedish Foundation for Strategic Research is acknowledged for funding through the SSF mobility grant SM23-0058. The work was performed in part at the Chalmers Materials Analysis Laboratory, CMAL.

Appendix A. Supplementary data

Supplementary data to this article can be found online at https://doi.org/10.1016/j.ijrmhm.2024.106810.

References

[1] P.C. Jindal, A.T. Santhanam, U. Schleinkofer, A.F. Shuster, Performance of PVD TiN, TiCN, and TiAlN coated cemented carbide tools in turning, Int. J. Refract. Met. Hard Mater. 17 (1999) 163–170, https://doi.org/10.1016/S0263-4368(99)00008-6.

[2] A. Inspektor, P.A. Salvador, Architecture of PVD coatings for metalcutting applications: a review, Surf. Coatings Technol. 257 (2014) 138–153, https://doi.org/10.1016/J.SURFCOAT.2014.08.068.

[3] J.H. Hsieh, A.L.K. Tan, X.T. Zeng, Oxidation and wear behaviors of Ti-based thin films, Surf. Coatings Technol. 201 (2006) 4094–4098, https://doi.org/10.1016/J.SURFCOAT.2006.08.026.

[4] K. Kutschej, P.H. Mayrhofer, M. Kathrein, P. Polcik, R. Tessadri, C. Mitterer, Structure, mechanical and tribological properties of sputtered Ti1–xAlxN coatings with 0.5≤x≤0.75, Surf. Coatings Technol. 200 (2005) 2358–2365, https://doi.org/10.1016/J.SURFCOAT.2004.12.008.

[5] D. Holec, R. Rachbauer, L. Chen, L. Wang, D. Luef, P.H. Mayrhofer, Phase stability and alloy-related trends in Ti–Al–N, Zr–Al–N and Hf–Al–N systems from first principles, Surf. Coatings Technol. 206 (2011) 1698–1704, https://doi.org/10.1016/J.SURFCOAT.2011.09.019.

[6] B. Grossmann, N. Schalk, C. Czettl, M. Pohler, C. Mitterer, Phase composition and thermal stability of arc evaporated $Ti_{1-x}Al_xN$ hard coatings with $0.4 \leq x \leq 0.67$, Surf. Coatings Technol. 309 (2017) 687–693, https://doi.org/10.1016/J.SURFCOAT.2016.11.015.

[7] M. Tkadletz, A. Lechner, N. Schalk, B. Sartory, A. Stark, N. Schell, C. Saringer, C. Mitterer, C. Czettl, Influence of spinodal decomposition and fcc→w phase transformation on global and local mechanical properties of nanolamellar CVD fcc-$Ti_{1-x}Al_xN$ coatings, Materialia 11 (2020) 100696, https://doi.org/10.1016/J.MTLA.2020.100696.

[8] J. Todt, R. Pitonak, A. Köpf, R. Weißenbacher, B. Sartory, M. Burghammer, R. Daniel, T. Schöberl, J. Keckes, Superior oxidation resistance, mechanical properties and residual stresses of an Al-rich nanolamellar $Ti_{0.05}Al_{0.95}N$ coating prepared by CVD, Surf. Coatings Technol. 258 (2014) 1119–1127, https://doi.org/10.1016/J.SURFCOAT.2014.07.022.

[9] A. Joshi, H.S. Hu, Oxidation behavior of titanium-aluminium nitrides, Surf. Coatings Technol. 76–77 (1995) 499–507, https://doi.org/10.1016/0257-8972(95)02566-9.

[10] F. Vaz, L. Rebouta, M. Andritschky, M.F. Da Silva, J.C. Soares, Thermal oxidation of $Ti_{1-x}Al_xN$ coatings in air, J. Eur. Ceram. Soc. 17 (1997) 1971–1977, https://doi.org/10.1016/S0955-2219(97)00050-2.

[11] I. Endler, M. Höhn, M. Herrmann, R. Pitonak, S. Ruppi, M. Schneider, H. van den Berg, H. Westphal, Novel aluminum-rich $Ti_{1-x}Al_xN$ coatings by LPCVD, Surf. Coatings Technol. 203 (2008) 530–533, https://doi.org/10.1016/J.SURFCOAT.2008.04.098.

[12] J. Keckes, R. Daniel, C. Mitterer, I. Matko, B. Sartory, A. Koepf, R. Weißenbacher, R. Pitonak, Self-organized periodic soft-hard nanolamellae in polycrystalline TiAlN thin films, Thin Solid Films 545 (2013) 29–32, https://doi.org/10.1016/J.TSF.2013.08.001.

[13] R. Qiu, O. Bäcke, D. Stiens, W. Janssen, J. Kümmel, T. Manns, H.O. Andrén, M. Halvarsson, CVD TiAlN coatings with tunable nanolamella architectures, Surf. Coatings Technol. 413 (2021) 127076, https://doi.org/10.1016/J.SURFCOAT.2021.127076.

[14] J. Todt, J. Zalesak, R. Daniel, R. Pitonak, A. Köpf, R. Weißenbacher, B. Sartory, C. Mitterer, J. Keckes, Al-rich cubic $Al_{0.8}Ti_{0.2}N$ coating with self-organized nanolamellar microstructure: thermal and mechanical properties, Surf. Coatings Technol. 291 (2016) 89–93, https://doi.org/10.1016/J.SURFCOAT.2016.02.027.

[15] R. Qiu, A. Forslund, O. Bäcke, A.H.S. Iyer, M. Sattari, W. Janssen, T. Manns, J. Kümmel, A. Ruban, D. Stiens, H.O. Andrén, M. Halvarsson, Effects of gas flow on detailed microstructure inhomogeneities in LPCVD TiAlN nanolamella coatings, Materialia 9 (2020) 100546, https://doi.org/10.1016/J.MTLA.2019.100546.

[16] A. Paseuth, Y. Kido, S. Imamura, K. Yamagata, A. Miura, K. Tadanaga, Thermal stability and cutting performance of Al-rich cubic $AlxTi_{1-x}N$ coating prepared by low-pressure chemical vapour deposition, J. Ceram. Soc. Japan 125 (2017) 913–918, https://doi.org/10.2109/JCERSJ2.17152.

[17] O. Bäcke, S. Kalbfleisch, D. Stiens, T. Manns, A. Davydok, M. Halvarsson, M. H. Colliander, Decomposition pathways in nano-lamellar CVD $Ti_{0.2}Al_{0.8}N$, Materialia 30 (2023) 101833, https://doi.org/10.1016/J.MTLA.2023.101833.

[18] M. Tkadletz, C. Hofer, C. Wüstefeld, N. Schalk, M. Motylenko, D. Rafaja, H. Holzschuh, W. Bürgin, B. Sartory, C. Mitterer, C. Czettl, Thermal stability of nanolamellar fcc-$Ti_{1-x}Al_xN$ grown by chemical vapor deposition, Acta Mater. 174 (2019) 195–205, https://doi.org/10.1016/J.ACTAMAT.2019.05.044.

[19] A. Paseuth, K. Yamagata, A. Miura, M. Higuchi, K. Tadanaga, Deposition and analysis of Al-rich c-$Al_xTi_{1-x}N$ coating with preferred orientation, J. Am. Ceram. Soc. 100 (2017) 343–353, https://doi.org/10.1111/JACE.14549.

[20] R. Qiu, H. Aboulfadl, O. Bäcke, D. Stiens, H.O. Andrén, M. Halvarsson, Atom probe tomography investigation of 3D nanoscale compositional variations in CVD TiAlN nanolamella coatings, Surf. Coatings Technol. 426 (2021) 127741, https://doi.org/10.1016/J.SURFCOAT.2021.127741.

[21] C. Saringer, M. Tkadletz, A. Stark, N. Schell, C. Czettl, N. Schalk, In-situ investigation of the oxidation behavior of metastable CVD-$Ti_{1-x}Al_xN$ using a novel combination of synchrotron radiation XRD and DSC, Surf. Coatings Technol. 374 (2019) 617–624, https://doi.org/10.1016/J.SURFCOAT.2019.05.072.

[22] M. Abdoos, B. Bose, S. Rawal, A.F.M. Arif, S.C. Veldhuis, The influence of residual stress on the properties and performance of thick TiAlN multilayer coating during dry turning of compacted graphite iron, Wear 454–455 (2020) 203342, https://doi.org/10.1016/J.WEAR.2020.203342.

[23] G. Skordaris, K.D. Bouzakis, T. Kotsanis, P. Charalampous, E. Bouzakis, B. Breidenstein, B. Bergmann, B. Denkena, Effect of PVD film's residual stresses on their mechanical properties, brittleness, adhesion and cutting performance of coated tools, CIRP J. Manuf. Sci. Technol. 18 (2017) 145–151, https://doi.org/10.1016/J.CIRPJ.2016.11.003.

[24] M. Meindlhumer, S. Klima, N. Jäger, A. Stark, H. Hruby, C. Mitterer, J. Keckes, R. Daniel, Stress-controlled decomposition routes in cubic AlCrN films assessed by in-situ high-temperature high-energy grazing incidence transmission X-ray diffraction, Sci. Reports 91 (9) (2019) 1–14, https://doi.org/10.1038/s41598-019-54307-7.

[25] N. Jäger, M. Meindlhumer, S. Spor, H. Hruby, J. Julin, A. Stark, F. Nahif, J. Keckes, C. Mitterer, R. Daniel, Microstructural evolution and thermal stability of AlCr(Si)N hard coatings revealed by in-situ high-temperature high-energy grazing incidence transmission X-ray diffraction, Acta Mater. 186 (2020) 545–554, https://doi.org/10.1016/J.ACTAMAT.2020.01.026.

[26] M. Moreno, J.M. Andersson, J. Eriksson, P. Alm, K. Hedström, R. M'Saoubi, I. C. Schramm, N. Schell, M. Johansson-Jöesaar, M. Odén, L. Rogström, Strain and phase evolution in TiAlN coatings during high-speed metal cutting: an in operando high-energy x-ray diffraction study, Acta Mater. (2023) 119538, https://doi.org/10.1016/J.ACTAMAT.2023.119538.

[27] J. Kieffer, V. Valls, N. Blanc, C. Hennig, New tools for calibrating diffraction setups, J. Synchrotron Radiat. 27 (2020) 558–566, https://doi.org/10.1107/S1600577520000776.
[28] P. Crowther, C. Daniel, xrdfit v. 1.3.0, GitHub Repos. https://github.com/LightForm-group/xrdfit, 2023.
[29] T. Manns, B. Scholtes, DECcalc - a program for the calculation of diffraction elastic constants from single crystal coefficients, Mater. Sci. Forum 681 (2011) 417–419, https://doi.org/10.4028/WWW.SCIENTIFIC.NET/MSF.681.417.
[30] N. Shulumba, O. Hellman, L. Rogström, Z. Raza, F. Tasnádi, I.A. Abrikosov, M. Odén, Temperature-dependent elastic properties of $Ti_{1-x}Al_xN$ alloys, Appl. Phys. Lett. 107 (2015) 231901, https://doi.org/10.1063/1.4936896.
[31] D.V. Suetin, I.R. Shein, A.L. Ivanovskii, Elastic and electronic properties of hexagonal and cubic polymorphs of tungsten monocarbide WC and mononitride WN from first-principles calculations, Phys. Status Solidi 245 (2008) 1590–1597, https://doi.org/10.1002/pssb.200844077.
[32] D.V. Suetin, I.R. Shein, A.L. Ivanovskii, Structural, electronic and magnetic properties of η carbides (Fe_3W_3C, Fe_6W_6C, Co_3W_3C and Co_6W_6C) from first principles calculations, Phys. B Condens. Matter 404 (2009) 3544–3549, https://doi.org/10.1016/J.PHYSB.2009.05.051.
[33] A. Taylor, R.W. Floyd, Precision Measurements of Lattice Parameters of Non-Cubic Crystals, Urn:Issn:0365-110X 3, 1950, pp. 285–289, https://doi.org/10.1107/S0365110X50000732.
[34] M. Hou, W. Mou, G. Yan, G. Song, Y. Wu, W. Ji, Z. Jiang, W. Wang, C. Qian, Z. Cai, Effects of different distribution of residual stresses in the depth direction on cutting performance of TiAlN coated WC-10wt%co tools in milling Ti-6Al-4V, Surf. Coatings Technol. 397 (2020) 125972, https://doi.org/10.1016/J.SURFCOAT.2020.125972.
[35] M. Hans, L. Patterer, D. Music, D.M. Holzapfel, S. Evertz, V. Schnabel, B. Stelzer, D. Primetzhofer, B. Völker, B. Widrig, A.O. Eriksson, J. Ramm, M. Arndt, H. Rudigier, J.M. Schneider, Stress-dependent elasticity of TiAlN coatings, Coatings 9 (2019) 24, https://doi.org/10.3390/COATINGS9010024.
[36] P.H. Mayrhofer, D. Music, J.M. Schneider, Influence of the Al distribution on the structure, elastic properties, and phase stability of supersaturated $Ti_{1-x}Al_xN$, J. Appl. Phys. 100 (2006) 94906, https://doi.org/10.1063/1.2360778.